

# PixARMesh: Autoregressive Mesh-Native Single-View Scene Reconstruction

Xiang Zhang<sup>\*,1,2,†</sup> Sohyun Yoo<sup>\*,1</sup> Hongrui Wu<sup>\*,1,‡</sup> Chuan Li<sup>2</sup> Jianwen Xie<sup>2</sup> Zhuowen Tu<sup>1</sup>  
<sup>1</sup>UC San Diego <sup>2</sup>Lambda, Inc.

\*equal contribution

## Abstract

We introduce *PixARMesh*, a method to autoregressively reconstruct complete 3D indoor scene meshes directly from a single RGB image. Unlike prior methods that rely on implicit signed distance fields and post-hoc layout optimization, *PixARMesh* jointly predicts object layout and geometry within a unified model, producing coherent and artist-ready meshes in a single forward pass. Building on recent advances in mesh generative models, we augment a point-cloud encoder with pixel-aligned image features and global scene context via cross-attention, enabling accurate spatial reasoning from a single image. Scenes are generated autoregressively from a unified token stream containing context, pose, and mesh, yielding compact meshes with high-fidelity geometry. Experiments on synthetic and real-world datasets show that *PixARMesh* achieves state-of-the-art reconstruction quality while producing lightweight, high-quality meshes ready for downstream applications.

## 1. Introduction

Reconstructing a complete 3D scene from a single RGB image is a long-standing and fundamentally ill-posed problem. A single viewpoint provides only partial, depth-ambiguous observations of objects, while large portions of the scene remain occluded or unobserved. Recovering accurate object shapes and coherent spatial layouts therefore requires strong priors about indoor scenes and plausible object structures.

Earlier methods [8, 9, 47] reconstruct the entire scene holistically by back-projecting image features into 3D volumes and predicting a scene-level signed distance field (SDF) using an encoder-decoder architecture. While these approaches bypass explicit layout estimation, they remain fundamentally constrained by the spatial resolution of volumetric grids and the limited expressiveness of feed-forward decoders. As a result, they struggle to produce high-quality

<sup>†</sup>Work partially done during internship at Lambda.

<sup>‡</sup>H. Wu contributed to the work during internship at UC San Diego.

Project page: <https://mlpc-ucsd.github.io/PixARMesh>

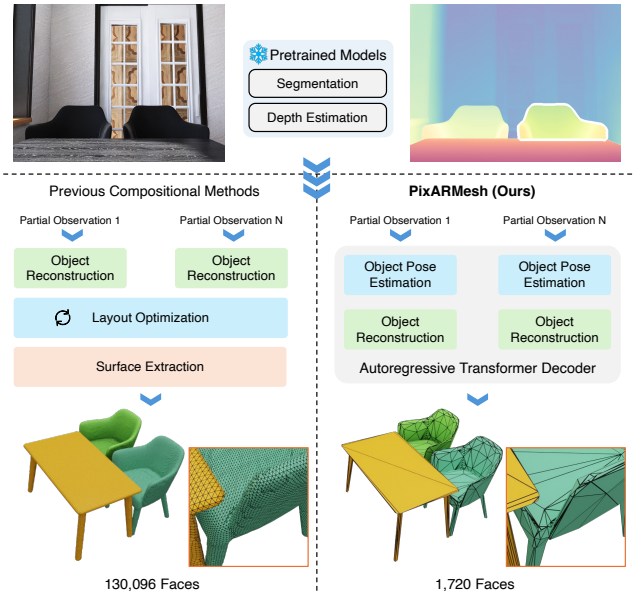


Figure 1. Comparison of PixARMesh with recent compositional scene reconstruction methods. PixARMesh predicts object poses and reconstructs native meshes in a single autoregressive decoding process, without relying on SDF-based surface extraction or layout optimization, producing compact and artist-ready mesh outputs.

geometry and lack the generative flexibility and generalization capability needed for complex real-world scenes.

Recently, the compositional generation paradigm has gained significant attention, driven by advances in large-scale object-level reconstruction models [18, 22, 29–31, 46]. Since these models are typically pre-trained on clean, unoccluded object images, existing pipelines [13, 51] require an inpainting or amodal completion stage to recover occluded regions before passing object crops to the reconstruction network. To assemble the reconstructed instances into a coherent scene, they further rely on optimization-based layout estimation, often formulated as point-cloud matching, which can be prone to local minima. Recent works such as DepR [49] mitigate the need for inpainting by conditioning generation directly on partial observations, while MIDI [19] eliminates layout optimization by predicting each instance directly in normalized scene coordinates. Although these methods generally achieve higher

reconstruction fidelity, their dependence on SDF-based representations introduces additional complexity in surface extraction and often yields overly smooth, high-face-count meshes that deviate from artist-ready geometry.

Meanwhile, there is steady progress in object-level mesh generative models [4–6, 25, 39, 41, 44, 48], where artist-like mesh sequences are directly predicted by an autoregressive Transformer decoder, eliminating the need for iso-surface extraction. However, despite these advances, autoregressive mesh generators remain limited to object-level outputs, and no existing scene reconstruction pipeline leverages their native, artist-ready mesh representations. This gap motivates the integration of strong partial observations with mesh-level generative priors for scene-level reconstruction.

To bridge this gap, we propose PixARMesh, a framework built on top of pre-trained object-level autoregressive mesh generative models such as EdgeRunner [41] and BPT [44], introducing a new paradigm for single-view scene reconstruction using native, artist-ready mesh representations. This architectural shift allows us to replace complex optimization loops with a unified, feed-forward autoregressive sequence (see Fig. 1), ensuring coherent scene composition and high-fidelity geometry. To leverage the limited geometric cues available in depth-back-projected point clouds, we fuse pixel-aligned image features into the point-cloud encoder, injecting appearance cues on top of partial geometry. To further enhance scene-level understanding, we incorporate cross-attention between each object’s point-cloud features and a global scene point cloud, enabling context-aware reconstruction under heavy occlusion. Finally, we utilize the coordinate vocabulary of existing mesh generative models to tokenize scene composition, allowing PixARMesh to jointly predict object poses and meshes within a single feed-forward autoregressive sequence. We validate PixARMesh on synthetic 3D-FRONT [14] and real-world images, demonstrating that it produces high-quality, artist-ready meshes with coherent layouts and strong reconstruction performance.

Our main contributions are summarized as follows:

- We present the first framework that performs single-view scene reconstruction *directly, autoregressively* in mesh space, avoiding SDF-based decoding and surface extraction while producing high-quality, artist-ready outputs.
- We repurpose recent object-level mesh generative models by incorporating *pixel-aligned image features* and *global scene context* into the point-cloud encoder, enabling context-aware pose and geometry generation from a single image.
- We jointly predict object poses and meshes in a single feed-forward autoregressive manner, achieving coherent scene composition without post-hoc layout optimization. Extensive experiments demonstrate PixARMesh achieves state-of-the-art reconstruction performance.

## 2. Related Work

**3D Scene Reconstruction from a Single Image** Single-view reconstruction is inherently ill-posed due to scale ambiguity, occlusion, and incomplete geometric cues, often requiring depth or shape priors from large-scale pre-trained models. Early holistic approaches such as Panoptic3D [32], PanoRe [9], Uni-3D [47], and BUOL [8] reconstruct an entire scene using feed-forward encoder-decoder architectures applied to back-projected feature volumes. While these methods do not require explicit layout estimation, they are constrained by limited spatial resolution and exhibit poor generalization and generative capability.

Recent research has shifted toward compositional generation frameworks that decompose a scene into individual instances and reconstruct them before composing the final scene. Some approaches [20, 23] rely on shape retrieval and procedural assembly, while others benefit from advances in object-level generative models. For example, Gen3DSR [13] and DeepPriorAssembly [51] perform image inpainting to complete occluded regions before feeding the recovered object crops into pre-trained object reconstruction models [22, 31, 45, 46]. DepR [49] instead generates shapes conditioned on partial image observations using a depth-guided diffusion model. These methods rely on post-hoc, optimization-based layout estimation to compose reconstructed instances back into a scene, which can be susceptible to local minima and spatial misalignment. MIDI [19] alleviates this limitation by generating all instances within a normalized scene space, thereby avoiding explicit pose estimation. Despite these advances, most existing approaches operate on signed distance fields (SDFs) and require iso-surface extraction via marching cubes [33], often producing densely tessellated and overly smooth meshes that hinder geometry-based applications such as editing. Our work addresses these limitations by unifying object layout prediction and mesh-native reconstruction into a single autoregressive sequence.

**Native Mesh Generation** Generating 3D shapes directly in native, artist-like meshes has long been attractive for their compactness, editability, and compatibility with downstream graphics applications. Early methods rely on structured primitives such as surface patches [16], deformable ellipsoids [42], mesh graphs [10], and binary space partitioning [7], but they typically impose strong geometric priors and offer limited topological flexibility. More recently, PolyDiff [1] applies discrete diffusion to synthesize meshes, while PolyGen [34] introduces an autoregressive framework that predicts vertices and faces using two coordinated Transformer decoders.

Subsequent approaches move to a single-sequence formulation. MeshGPT [39] employs a Transformer over VQ-VAE-quantized mesh tokens, and MeshAnything [5] ex-

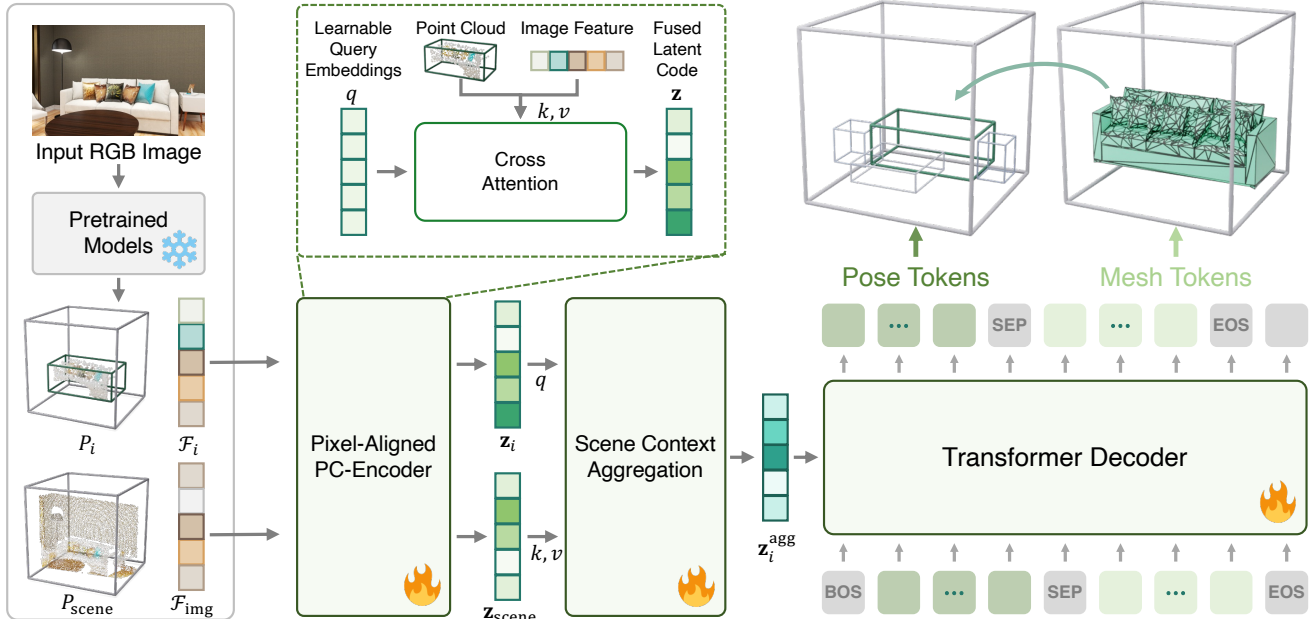


Figure 2. Pipeline overview. Given an RGB image, we use pretrained models to extract the depth point cloud and image features for both the target object  $i$  and the global scene. These local and global cues are fed into the Pixel-Aligned PC-Encoder to produce the fused latent code, which is then aggregated into a single latent vector via cross-attention. This latent vector conditions the Transformer Decoder, which predicts the object’s pose followed by its mesh token sequence.

tends it with shape-conditional generation. MeshXL [4] further simplifies the process by operating directly in quantized coordinate space, removing the need for a VQ-VAE but at the cost of longer token sequences. To improve scalability, recent studies propose compressive tokenization strategies that exploit face adjacency [6, 26, 41, 44]. Meshtron [17] follows MeshXL tokenization but introduces an Hourglass Transformer [35] to internally compress long sequences.

Others explore complementary directions for improving mesh generation quality and controllability. DeepMesh [50] and Mesh-RFT [28] incorporate reinforcement learning to align mesh generation with aesthetic or human preferences. PivotMesh [43] generates pivot vertices as coarse structural guidance for subsequent mesh generation, while VertexRegen [48] and ARMesh [25] advance the coarse-to-fine generation paradigm by progressively increasing geometric detail. Building on mesh generative models with strong compression and scalability, such as EdgeRunner [41] and BPT [44], our work extends these advances to scene-level reconstruction with artist-like meshes.

### 3. Method

We provide an overview of our framework in Fig. 2, which consumes depth-derived point clouds from off-the-shelf perception models and performs autoregressive scene reconstruction. We first introduce the problem setup in Sec. 3.1, then describe how we adapt point-cloud encoders

from object-level mesh generative models to operate at the scene level. Finally, we detail our tokenization scheme in Sec. 3.3 and our training strategy in Sec. 3.4.

#### 3.1. Preliminary

The goal of single-view scene reconstruction is to recover the 3D geometry and spatial configuration of a scene from a single RGB image. Following the compositional paradigm used in prior work such as DepR [49] and DeepPriorAssembly [51], we focus on reconstructing only foreground object instances (e.g. furniture in indoor scenes) and disregard large planar background structures such as walls and floors.

We introduce PixARMesh, an end-to-end framework that jointly predicts the shape and scene-level pose of each object instance, producing a complete scene where all objects are represented using native, artist-ready meshes rather than implicit SDFs.

Given an input RGB image  $I \in \mathbb{R}^{H \times W \times 3}$ , we first extract depth  $D$ , instance segmentation masks  $\mathcal{M} = \{M_i\}_{i=1}^N$ , and image features  $\mathcal{F}_{img}$  using off-the-shelf models. The depth map is back-projected using the camera intrinsics  $K$  to obtain a raw scene point cloud  $P_{scene}$ . Applying the instance masks yields per-object point clouds  $\mathcal{P} = \{P_i\}_{i=1}^N$  where  $P_i = P_{scene} \odot M_i$ , which capture only the visible portions of each object in global camera coordinates.

Unlike previous compositional methods that reconstruct object shapes first and resolve their spatial layout afterward,

we unify both tasks in a single autoregressive feed-forward architecture. For each instance  $i$ , the model  $F_{\text{AR}}$  predicts both its scene-level pose  $T_i$  and its canonical mesh  $O_i$ :

$$(T_i, O_i) = F_{\text{AR}}(P_i, M_i, \mathcal{F}_{\text{img}}, P_{\text{scene}}) \quad (1)$$

After processing all instances, the final scene reconstruction is obtained by transforming each canonical mesh into the scene coordinate frame  $\mathcal{S} = \{T_i O_i\}_{i=1}^N$ .

We adopt EdgeRunner [41] and BPT [44] as our base models, both of which are autoregressive mesh generators designed for object-level, shape-conditioned generation. In their original formulations, a point-cloud encoder processes *complete object point clouds* and produces conditioning tokens for the Transformer decoder to autoregressively generate mesh sequences. However, in single-view scene reconstruction, objects are only partially observed due to occlusions, and their global poses within the scene must also be inferred. In the following sections, we describe how we repurpose them for the single-view setting by (1) adapting the point-cloud encoder to incorporate appearance features from an image encoder, (2) injecting global scene context to compensate for missing geometry, and (3) predicting object poses within the same autoregressive framework.

### 3.2. Repurposing the Point-Cloud Encoder

**Injecting Pixel-Aligned Image Features** The original point-cloud encoder used in EdgeRunner and BPT operates solely on point coordinates, without leveraging the rich appearance cues present in image features. To support single-view reconstruction, where objects are often partially observed, we augment the encoder with direct multi-modal fusion between geometry and pixel-aligned image features.

Given an instance point cloud  $P_i$  and camera intrinsics  $K$ , each 3D point  $p$  is projected onto the image plane to obtain its corresponding pixel  $\text{Proj}(K, p) = (u, v)$  on the global feature map  $\mathcal{F}_{\text{img}}$ , establishing a point-pixel correspondence. For each such pair, the encoder  $\mathcal{E}_{\text{pc}}$  concatenates the geometric feature  $\mathbf{f}_p^{\text{pc}}$  with the aligned image feature  $\mathbf{f}_p^{\text{img}} = \mathcal{F}_{\text{img}}(u, v)$  to form the key-value inputs to a Transformer-based fusion block. A set of learnable query embeddings then aggregates these fused features into a compact latent code:

$$\mathbf{z}_i = \mathcal{E}_{\text{pc}}(\mathbf{f}_p^{\text{pc}}, \mathbf{f}_p^{\text{img}}) \quad \forall p \in P_i. \quad (2)$$

This pixel-aligned design enables the autoregressive mesh generator to incorporate per-point appearance cues, enhancing robustness to occlusion and improving the completeness and global consistency of the reconstructed geometry.

**Scene Context Aggregation** Instead of normalizing each instance independently in its own canonical space, which discards global spatial relations, we first normalize the entire global point cloud  $P_{\text{scene}}$  and all instance point clouds

$\{P_i\}_{i=1}^N$  into a unified scene coordinate frame. This preserves consistent spatial reference among all objects. The normalized instance point clouds are then fed into the pixel-aligned point cloud encoder, ensuring that all encoded features share a coherent spatial frame for subsequent context aggregation. From this encoder, we obtain a scene-level latent  $\mathbf{z}_{\text{scene}}$  and per-instance latent codes  $\mathbf{z}_i$ .

To incorporate global scene context, *e.g.*, cues from nearby objects of similar category or geometry, and to further improve reconstruction quality, each object latent  $\mathbf{z}_i$  attends to the scene-level latent via a cross-attention layer:

$$\mathbf{z}_i^{\text{agg}} = \text{CrossAttn}(q = \mathbf{z}_i, k = \mathbf{z}_{\text{scene}}, v = \mathbf{z}_{\text{scene}}), \quad (3)$$

The resulting aggregated feature  $\mathbf{z}_i^{\text{agg}}$  enriches the instance representation with holistic scene cues, enabling more accurate pose estimation and geometry prediction.

### 3.3. Tokenization

As an autoregressive framework, our model represents both object poses and meshes as discrete tokens. We uniformly quantize the unit cube  $[-1, 1]^3$  into  $N$  bins along each axis. For EdgeRunner, each vertex is represented by three integer tokens  $\langle x \rangle$ ,  $\langle y \rangle$ ,  $\langle z \rangle$ , while BPT replaces these with a  $\langle \text{block\_id} \rangle$  and  $\langle \text{offset\_id} \rangle$  pair through block-wise decomposition of the  $N^3$  quantized grid.

**Object Pose Tokenization** Following standard conventions in 3D detection [24], we represent each object pose using a gravity-aligned 7-DoF bounding box (center, scale, yaw). Rather than introducing a separate vocabulary for pose parameters (*e.g.*, the yaw angle), we reuse the vertex tokenization scheme by encoding the 8 corner points of the bounding box (normalized with respect to the global normalization in Sec. 3.2). This yields lightweight pose sequences (24 tokens for EdgeRunner and 16 tokens for BPT), negligible compared to mesh sequences. Importantly, this vertex-based formulation enables complete vocabulary sharing with mesh tokenization, avoiding new token types while maintaining expressiveness.

At inference time, the pose sequence is decoded into 8 bounding-box corners in the normalized scene coordinate frame. The subsequent mesh sequence is decoded in the local canonical space, where each object is normalized to a unit cube. To bridge these two spaces, we recover a local-to-global transformation using the decoded global-space corners as targets. Let  $\mathbf{X}_{\text{local}} \in \mathbb{R}^{8 \times 3}$  denote the canonical box corners and  $\mathbf{X}_{\text{global}} \in \mathbb{R}^{8 \times 3}$  denote the decoded global-space corners. We estimate the best-fit affine transformation  $\mathbf{T} \in \mathbb{R}^{3 \times 4}$  by solving the linear least-squares problem:

$$\mathbf{T}^* = \arg \min_{\mathbf{T}} \|\mathbf{X}_{\text{global}} - [\mathbf{X}_{\text{local}} \mathbf{1}] \mathbf{T}^{\top}\|_2^2. \quad (4)$$

The resulting transformation  $\mathbf{T}^*$  is interpreted as a gravity-aligned transform, and is applied to all vertices of the de-

coded canonical mesh, yielding the final object geometry in the global scene frame.

**Object Mesh Tokenization** For mesh sequences, we adopt the native tokenization strategy of each base model.

BPT uses a *Blocked and Patchified Tokenization* scheme that partitions the 3D coordinate grid into blocks and aggregates spatially adjacent faces into compact patches. This achieves strong compression (ratio  $\approx 0.26$  at resolution 128) with a large, structured vocabulary of 40,960 tokens.

EdgeRunner employs a *Compact Mesh Tokenization* derived from the EdgeBreaker algorithm [38], traversing triangles via a half-edge structure to maximize vertex reuse. It attains a moderate compression ratio ( $\approx 0.46$  at resolution 512) with a smaller vocabulary of 518 tokens, while preserving high geometric fidelity.

These two tokenization paradigms are complementary: BPT prioritizes aggressive sequence compression with a high-capacity vocabulary, whereas EdgeRunner emphasizes resolution and geometric detail with a more compact vocabulary and moderate compression. In all cases, meshes are normalized to a unit cube and vertex coordinates are discretized according to the respective quantization resolution. Our framework supports both without modification, demonstrating robustness to widely different tokenization designs.

**Final Token Sequence** For each object, the final autoregressive sequence is constructed as:

`<bos>, [pose_seq], <sep>, [mesh_seq], <eos>`

where `[pose_seq]` and `[mesh_seq]` denote the tokenized pose and mesh sequences, respectively.

### 3.4. Training

Our autoregressive decoder is trained using a single next-token prediction objective. Given a token sequence  $S = (s_1, \dots, s_T)$  and aggregated latent  $\mathbf{z}_{\text{agg}}$ , the training loss is

$$\mathcal{L}_{\text{ce}} = - \sum_{t=1}^T \log p_{\theta}(s_t | s_{<t}, \mathbf{z}_{\text{agg}}), \quad (5)$$

where the model predicts each token conditioned on all preceding tokens and the fused point-cloud latent augmented with pixel-aligned image features and global scene context.

As illustrated in Fig. 2, the model autoregressively generates both the pose tokens and the mesh tokens within a single unified sequence. This joint formulation allows the decoder to learn instance geometry and global layout estimation simultaneously, enabling pose reasoning to benefit from geometry cues and vice versa.

## 4. Experiments

### 4.1. Settings

**Datasets** We conduct experiments on synthetic and real-world datasets. For training, we use the synthetic indoor

dataset 3D-FRONT [14], adopting the preprocessed version provided by InstPIFu [27]. Since the raw 3D-FRONT meshes are high-poly, we apply planar decimation to all object assets to obtain lightweight, artist-compatible meshes suitable for autoregressive generation. Additional preprocessing details are provided in the supplementary material. 3D-FRONT contains over 16K object meshes sourced from 3D-FUTURE [15], along with scene layouts, RGB images, depth maps, and instance segmentation masks.

Following the standard protocol, our training split consists of 22,673 scene images. For evaluation on synthetic data, we use the test subset curated by DepR [49], which includes 100 scenes for object-level and 156 scenes for scene-level evaluation.

To demonstrate real-world generalization, we additionally evaluate our model on images from Pix3D [40], Matterport3D [3], and ScanNet [11]. For these inputs, we employ Perspective Fields [21] to estimate camera intrinsics and pitch angles.

**Implementation Details** For 2D visual priors, we follow DepR [49] and employ off-the-shelf models: GroundedSAM [37] for instance segmentation, Depth Pro [2] for monocular depth estimation, and DINOv2 with register tokens [12, 36] as our image feature encoder.

For back-projected point clouds, we adopt the native sampling densities of each base mesh generative model: BPT-based models use 4,096 points per object, whereas EdgeRunner-based models use 8,192 points. For the global scene representation, we uniformly sample 16,384 points.

All point clouds (partial object-level and full scene-level) and object poses are normalized to a unit cube. We apply random augmentation during training, including a rotation along the vertical axis in the range  $[-45^\circ, 45^\circ]$ , scaling in  $[0.75, 1]$ , and shift in  $[0, 0.2]$ . We additionally jitter depth values by up to 0.02 to account for inaccuracies in monocular depth estimation. Object meshes are normalized to a unit cube in their respective canonical space.

We train all models on 8 NVIDIA H100 GPUs using AdamW with a learning rate of  $1 \times 10^{-4}$ , 500 warm-up iterations, and cosine decay. The BPT-based variant converges in roughly 18 hours, while the EdgeRunner-based variant requires around 2 days due to its substantially longer token sequence length.

**Evaluation Metrics** We evaluate our method using Chamfer Distance (CD) and F-Score, following standard practice in single-view reconstruction [27, 49, 51]. Unless otherwise noted, we use an F-Score threshold of 0.002. Each reconstructed mesh is uniformly sampled into 10k points prior to metric computation.

At the object level, we normalize predicted and ground-truth meshes to a unit cube and compute CD and F-Score to measure the geometric fidelity of individual objects.

At the scene level, we first assemble all predicted in-

Method	Scene-level			Object-level	
	CD ( $\times 10^{-3}$ , ↓)	CD-S ( $\times 10^{-3}$ , ↓)	F-Score (% , ↑)	CD ( $\times 10^{-3}$ , ↓)	F-Score (% , ↑)
SDF-based					
InstPIFu [27]	213.4	124.9	13.72	44.74	29.63
Uni-3D [47]	218.3	113.3	12.99	—	—
Gen3DSR [13]	222.4	137.5	13.52	9.74	31.42
DeepPriorAssembly [51]	191.8	76.2	16.72	20.13	27.83
MIDI [19]	156.3	79.3	24.83	6.71	72.69
DepR [49]	153.2	56.4	25.00	<b>2.57</b>	<b>89.66</b>
Mesh-based					
<b>PixARMesh-EdgeRunner (Ours)</b>	98.8	49.1	<b>33.55</b>	4.04	82.27
<b>PixARMesh-BPT (Ours)</b>	<b>98.4</b>	<b>47.6</b>	32.26	4.57	80.30

Table 1. Qualitative comparison with state-of-the-art methods on the 3D-FRONT [14] dataset. Following DepR [49] and DeepPriorAssembly [51], we report object- and scene-level Chamfer Distance (CD; lower is better) and F-Score (higher is better). We additionally include the single-direction Chamfer Distance (CD-S) to account for missing instances.

stances using their estimated poses. The composed scene, formed by placing each generated mesh into its predicted bounding box, remains in the normalized scene space described in Sec. 3.2. For fair comparison, we apply a global scale and translation to align the predicted scene with the ground-truth scene, which preserves its original metric scale and coordinate frame. Following DeepPriorAssembly [51], we additionally report the single-direction Chamfer Distance (CD-S), which emphasizes reconstruction completeness while ignoring empty background regions.

## 4.2. Main Results

**Quantitative Results** Tab. 1 reports quantitative comparisons on the synthetic 3D-FRONT [14] dataset. We benchmark PixARMesh against representative single-view scene reconstruction approaches, including diffusion-based methods such as DepR [49] and MIDI [19], feed-forward reconstruction frameworks such as InstPIFu [27], and holistic scene methods such as Uni-3D [47]. Because holistic models do not explicitly generate individual object meshes, object-level metrics are not applicable.

Our method achieves highly competitive performance at both the object and scene levels. At the object level, PixARMesh achieves the second-best performance among all approaches, with F-Score comparable to diffusion-based SDF models. Unlike SDF-based pipelines that require Marching Cubes to extract dense iso-surfaces, our approach directly produces compact, artist-ready meshes with only a few thousand faces per instance while maintaining comparable geometric precision. Further statistics on face counts are provided in the supplementary material. At the scene level, our method achieves state-of-the-art performance across all reported metrics. We attribute this to our unified autoregressive framework that jointly predicts object geometry and pose, leveraging our pixel-aligned point cloud encoder and scene-level context aggregation for coherent full-scene reconstruction. We also observe that the EdgeRunner-based variant delivers stronger reconstruction

performance than the BPT-based variant.

**Qualitative Results** We present qualitative comparisons on the synthetic 3D-FRONT [14] dataset in Fig. 3 and on real-world images in Fig. 4.

Across both synthetic and real settings, PixARMesh produces geometrically coherent scene reconstructions, capturing object shapes and spatial arrangements that generally correspond to the input images. Owing to the native artist-ready mesh representation, PixARMesh yields meshes with clear edges and well-defined structural boundaries while maintaining smooth surface continuity, leading to cleaner shapes compared to prior approaches.

On real-world images, PixARMesh shows reasonable generalization and can reconstruct indoor environments with practical and interpretable geometry, despite being trained primarily on synthetic data.

## 4.3. Ablation Studies

We conduct ablations on the 3D-FRONT [14] dataset to evaluate the effectiveness of PixARMesh. Our analysis focuses on two aspects: (1) pipeline design – examining the contribution of joint pose-mesh modeling and each proposed component, and (2) error analysis – investigating the impact of upstream perception errors on overall scene reconstruction performance. We use EdgeRunner-based variant with pixel-aligned image features and scene context aggregation, unless otherwise stated.

Method	Scene-level			Object-level	
	CD ( $\times 10^{-3}$ , ↓)	CD-S ( $\times 10^{-3}$ , ↓)	F-Score (% , ↑)	CD ( $\times 10^{-3}$ , ↓)	F-Score (% , ↑)
Two-stage	99.8	50.6	33.32	4.75	80.85
EdgeRunner-FT	119.8	48.0	27.81	4.75	80.57
<b>PixARMesh (Ours)</b>	<b>98.8</b>	<b>49.1</b>	<b>33.55</b>	<b>4.04</b>	<b>82.27</b>

Table 2. Ablation study on joint pose-mesh modeling.

**Necessity of Joint Pose-Mesh Modeling** We construct additional baselines to validate the effectiveness of the proposed joint modeling of object poses and meshes introduced in Sec. 3.3. The results are summarized in Tab. 2.



Figure 3. Qualitative comparisons on the 3D-FRONT [14] dataset. For PixARMesh, we also show the mesh wireframe to highlight geometric quality.

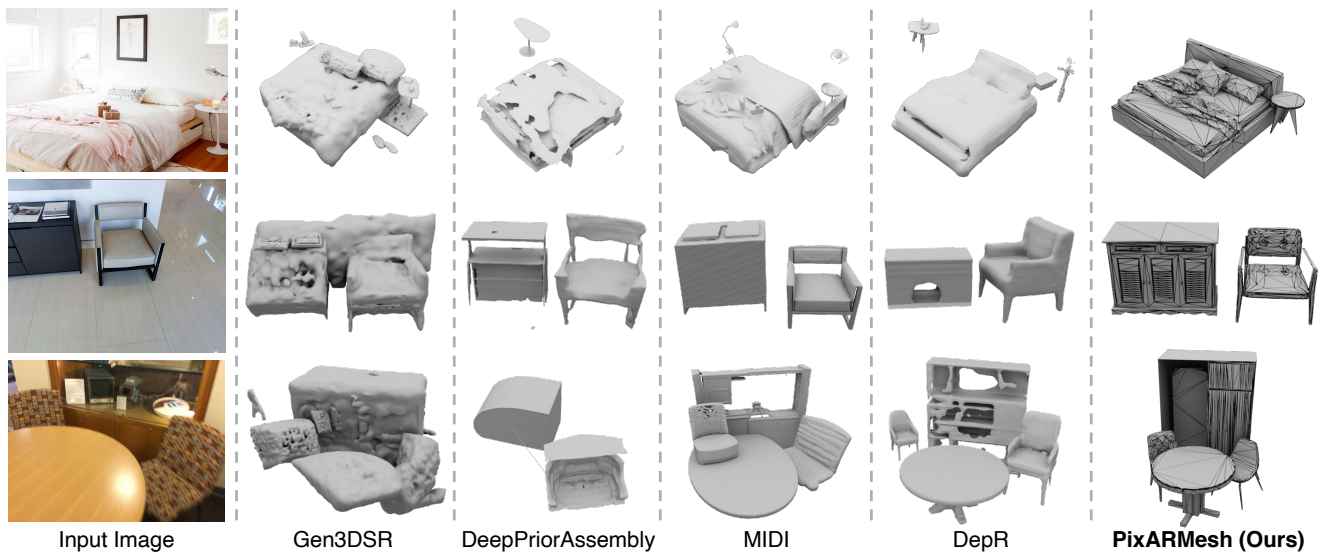


Figure 4. Qualitative results on real images from Pix3D [40], Matterport3D [3], and ScanNet [11] datasets.

The *EdgeRunner-FT* baseline is a fine-tuned EdgeRunner that reconstructs objects without layout conditions and composes scenes using the optimization strategy from DepR [49]. It notably underperforms PixARMesh at the scene level, highlighting that explicit layout prediction is fundamentally more effective than post-hoc optimization.

The *Two-stage* baseline decouples layout prediction and layout-conditioned mesh generation into separate models. Despite doubling the parameter count, it yields inferior performance across both scene-level and object-level metrics. In particular, joint modeling improves object reconstruction quality (CD 4.75  $\rightarrow$  4.04, F-Score 80.85  $\rightarrow$  82.27), suggesting that geometry generation benefits from being jointly optimized with pose prediction. While the two-stage design treats layout as a static condition, breaking the reasoning chain between localization and geometry, our unified formulation allows mesh generation to emerge as a coherent continuation of spatial reasoning.

Img Feat	Ctx Agg	Scene-level			Object-level	
		CD ( $\times 10^{-3}$ , $\downarrow$ )	CD-S ( $\times 10^{-3}$ , $\downarrow$ )	F-Score (%, $\uparrow$ )	CD ( $\times 10^{-3}$ , $\downarrow$ )	F-Score (%, $\uparrow$ )
		57.78	23.75	41.02	5.29	77.22
	✓	55.44	27.16	42.84	5.56	78.14
✓		<b>39.30</b>	<b>16.12</b>	44.67	<b>3.64</b>	<b>84.64</b>
✓	✓	39.88	18.52	<b>46.15</b>	4.04	82.27

Table 3. Ablation studies on our point-cloud encoder design. *Img Feat*, *Ctx Agg* denote pixel-aligned image features and scene context aggregation, respectively.

**Point-cloud Encoder Design** To validate our repurposed point-cloud encoder, we report results with predicted depth and ground-truth masks in Tab. 3; additional results for the BPT-based variant are provided in the supplementary.

Removing the pixel-aligned image features causes the largest performance drop in both object and scene-level metrics. While using image features alone yields the highest object-level fidelity and the lowest scene-level Chamfer Distance, it falls short of the full model in terms of scene-level F-Score. These results highlight the importance of pixel-aligned image features for geometric accuracy and the synergy provided by scene-level context for overall reconstruction completeness.

GT Depth	GT Layout	CD ( $\times 10^{-3}$ , $\downarrow$ )	F-Score (%, $\uparrow$ )
		4.13	81.64
✓		3.04	86.66
	✓	4.04	82.27
✓	✓	<b>2.93</b>	<b>87.19</b>

Table 4. Effects of depth and layout in object-level metrics.

**Object-Level Error Analysis** To assess the upper-bound potential of PixARMesh and the impact of upstream perception errors, we evaluate it using ground-truth depth and layout for object-level reconstruction. As shown in Tab. 4, replacing estimated depth with ground-truth depth provides the most significant boost in performance, reducing the Chamfer Distance from 4.13 to 3.04 and increasing the F-

Score from 81.64% to 86.66%. While providing ground-truth layout alone yields more modest gains (82.27% F-Score), the combination of both ground-truth depth and layout achieves the highest geometric fidelity with an F-Score of 87.19%. These results indicate that while PixARMesh is robust to imperfect inputs, accurate depth and layout estimation offer essential guidance for generating the highest-quality mesh sequences.

Depth	GT Inputs		CD ( $\times 10^{-3}$ , $\downarrow$ )	CD-S ( $\times 10^{-3}$ , $\downarrow$ )	F-Score (%, $\uparrow$ )
	Segm	Layout			
			98.84	49.08	33.55
✓			95.69	48.18	39.04
	✓		39.88	18.52	46.15
	✓	✓	16.30	4.40	63.91
✓	✓		25.07	10.05	59.63
✓	✓	✓	<b>13.25</b>	<b>3.52</b>	<b>68.48</b>

Table 5. Effects of upstream (depth, segmentation, and layout) errors in scene-level metrics. Note that ground-truth layout implies ground-truth segmentation.

**Scene-Level Error Analysis** To isolate the influence of imperfect 2D visual priors, we evaluate PixARMesh using various combinations of ground-truth (GT) inputs. As shown in Tab. 5, providing GT segmentation yields the most substantial single-module improvement, boosting the scene-level F-Score from 33.55% to 46.15%. This sensitivity suggests that corrupted instance masks, which may lead to missing objects or fragmented point clouds, represent the primary bottleneck for scene-level reconstruction.

The results further indicate that the model exhibits robustness to monocular depth inaccuracies. Incorporating GT depth alone improves the F-Score from 33.55% to 39.04%, but its impact is less pronounced compared to the gains from idealized segmentation. Ultimately, the system achieves its peak performance with an F-Score of 68.48% when all inputs are provided by an oracle. This demonstrates that while PixARMesh handles imperfect perception well, it scales effectively as upstream modules improve.

## 5. Conclusion

We presented PixARMesh, an autoregressive framework for single-view indoor scene reconstruction. By repurposing object-level mesh generative models with pixel-aligned image features and scene-level context aggregation, PixARMesh jointly predicts object pose and geometry, producing coherent full-scene reconstructions without relying on SDFs or post-hoc layout optimization. Our method achieves competitive object-level accuracy and state-of-the-art scene-level performance, notably while generating compact, artist-ready meshes. Extensive experiments and ablation studies highlight the effectiveness of our design and its applicability to real-world inputs, demonstrating the promise of autoregressive mesh generation as a viable alternative to conventional SDF-based pipelines.

## Acknowledgment

This work is supported by NSF award IIS-2127544 and NSF award IIS-2433768. We thank Lambda, Inc. for their compute resource help.

## References

- [1] Antonio Alliegro, Yawar Siddiqui, Tatiana Tommasi, and Matthias Nießner. Polydiff: Generating 3d polygonal meshes with diffusion models. *arXiv preprint arXiv:2312.11417*, 2023. 2
- [2] Alexey Bochkovskiy, Amaël Delaunoy, Hugo Germain, Marcel Santos, Yichao Zhou, Stephan Richter, and Vladlen Koltun. Depth pro: Sharp monocular metric depth in less than a second. In *The Thirteenth International Conference on Learning Representations*, 2025. 5
- [3] Angel Chang, Angela Dai, Thomas Funkhouser, Maciej Halber, Matthias Niebner, Manolis Savva, Shuran Song, Andy Zeng, and Yinda Zhang. Matterport3d: Learning from rgb-d data in indoor environments. In *2017 International Conference on 3D Vision*, pages 667–676. IEEE Computer Society, 2017. 5, 7, 12, 13
- [4] Sijin Chen, Xin Chen, Anqi Pang, Xianfang Zeng, Wei Cheng, Yijun Fu, Fukun Yin, Billzb Wang, Jingyi Yu, Gang Yu, et al. Meshxl: Neural coordinate field for generative 3d foundation models. *Advances in Neural Information Processing Systems*, 37:97141–97166, 2024. 2, 3
- [5] Yiwen Chen, Tong He, Di Huang, Weicai Ye, Sijin Chen, Jiaxiang Tang, Zhongang Cai, Lei Yang, Gang Yu, Guosheng Lin, and Chi Zhang. Meshanything: Artist-created mesh generation with autoregressive transformers. In *The Thirteenth International Conference on Learning Representations*, 2025. 2
- [6] Yiwen Chen, Yikai Wang, Yihao Luo, Zhengyi Wang, Zilong Chen, Jun Zhu, Chi Zhang, and Guosheng Lin. Meshanything v2: Artist-created mesh generation with adjacent mesh tokenization. In *Proceedings of the IEEE/CVF International Conference on Computer Vision*, pages 13922–13931, 2025. 2, 3
- [7] Zhiqin Chen, Andrea Tagliasacchi, and Hao Zhang. Bsp-net: Generating compact meshes via binary space partitioning. In *Proceedings of the IEEE/CVF conference on computer vision and pattern recognition*, pages 45–54, 2020. 2
- [8] Tao Chu, Pan Zhang, Qiong Liu, and Jiaqi Wang. Buol: A bottom-up framework with occupancy-aware lifting for panoptic 3d scene reconstruction from a single image. In *Proceedings of the IEEE/CVF Conference on Computer Vision and Pattern Recognition*, pages 4937–4946, 2023. 1, 2, 12, 13
- [9] Manuel Dahnert, Ji Hou, Matthias Nießner, and Angela Dai. Panoptic 3d scene reconstruction from a single rgb image. *Advances in Neural Information Processing Systems*, 34: 8282–8293, 2021. 1, 2
- [10] Angela Dai and Matthias Nießner. Scan2mesh: From unstructured range scans to 3d meshes. In *Proceedings of the IEEE/CVF Conference on Computer Vision and Pattern Recognition*, pages 5574–5583, 2019. 2
- [11] Angela Dai, Angel X Chang, Manolis Savva, Maciej Halber, Thomas Funkhouser, and Matthias Nießner. Scannet: Richly-annotated 3d reconstructions of indoor scenes. In *Proceedings of the IEEE Conference on Computer Vision and Pattern Recognition*, pages 5828–5839, 2017. 5, 7, 12, 13
- [12] Timothée Darcet, Maxime Oquab, Julien Mairal, and Piotr Bojanowski. Vision transformers need registers. In *The Twelfth International Conference on Learning Representations*, 2024. 5
- [13] Andreea Dogaru, Mert Özer, and Bernhard Egger. Gen3DSR: Generalizable 3d scene reconstruction via divide and conquer from a single view. In *International Conference on 3D Vision 2025*, 2025. 1, 2, 6, 12, 13
- [14] Huan Fu, Bowen Cai, Lin Gao, Ling-Xiao Zhang, Jiaming Wang, Cao Li, Qixun Zeng, Chengyue Sun, Rongfei Jia, Binqiang Zhao, and Hao Zhang. 3d-front: 3d furnished rooms with layouts and semantics. In *Proceedings of the IEEE/CVF International Conference on Computer Vision*, pages 10933–10942, 2021. 2, 5, 6, 7, 12
- [15] Huan Fu, Rongfei Jia, Lin Gao, Mingming Gong, Binqiang Zhao, Steve Maybank, and Dacheng Tao. 3d-future: 3d furniture shape with texture. *International Journal of Computer Vision*, 129(12):3313–3337, 2021. 5
- [16] Thibault Groueix, Matthew Fisher, Vladimir G Kim, Bryan C Russell, and Mathieu Aubry. A papier-mâché approach to learning 3d surface generation. In *Proceedings of the IEEE Conference on Computer Vision and Pattern Recognition*, pages 216–224, 2018. 2
- [17] Zekun Hao, David W Romero, Tsung-Yi Lin, and Ming-Yu Liu. Meshtron: High-fidelity, artist-like 3d mesh generation at scale. *arXiv preprint arXiv:2412.09548*, 2024. 3
- [18] Yicong Hong, Kai Zhang, Jiuxiang Gu, Sai Bi, Yang Zhou, Difan Liu, Feng Liu, Kalyan Sunkavalli, Trung Bui, and Hao Tan. LRM: Large reconstruction model for single image to 3d. In *The Twelfth International Conference on Learning Representations*, 2024. 1
- [19] Zehuan Huang, Yuan-Chen Guo, Xingqiao An, Yunhan Yang, Yangguang Li, Zi-Xin Zou, Ding Liang, Xihui Liu, Yan-Pei Cao, and Lu Sheng. Midi: Multi-instance diffusion for single image to 3d scene generation. In *Proceedings of the IEEE/CVF Conference on Computer Vision and Pattern Recognition*, pages 23646–23657, 2025. 1, 2, 6, 12, 13
- [20] Zhening Huang, Xiaoyang Wu, Fangcheng Zhong, Hengshuang Zhao, Matthias Nießner, and Joan Lasenby. Lite-reality: Graphic-ready 3d scene reconstruction from RGB-d scans. In *The Thirty-ninth Annual Conference on Neural Information Processing Systems*, 2025. 2
- [21] Linyi Jin, Jianming Zhang, Yannick Hold-Geoffroy, Oliver Wang, Kevin Blackburn-Matzen, Matthew Sticha, and David F Fouhey. Perspective fields for single image camera calibration. In *Proceedings of the IEEE/CVF Conference on Computer Vision and Pattern Recognition*, pages 17307–17316, 2023. 5
- [22] Heewoo Jun and Alex Nichol. Shap-e: Generating conditional 3d implicit functions. *arXiv preprint arXiv:2305.02463*, 2023. 1, 2

- [23] Weicheng Kuo, Anelia Angelova, Tsung-Yi Lin, and Angela Dai. Mask2cad: 3d shape prediction by learning to segment and retrieve. In *European Conference on Computer Vision*, pages 260–277. Springer, 2020. 2
- [24] Justin Lazarow, David Griffiths, Gefen Kohavi, Francisco Crespó, and Afshin Dehghan. Cubify anything: Scaling indoor 3d object detection. In *Proceedings of the IEEE/CVF Conference on Computer Vision and Pattern Recognition*, pages 22225–22233, 2025. 4
- [25] Jiabao Lei, Kewei Shi, Zhihao Liang, and Kui Jia. ARMesh: Autoregressive mesh generation via next-level-of-detail prediction. In *The Thirty-ninth Annual Conference on Neural Information Processing Systems*, 2025. 2, 3
- [26] Stefan Lionar, Jiabin Liang, and Gim Hee Lee. Treemeshgpt: Artistic mesh generation with autoregressive tree sequencing. In *Proceedings of the IEEE/CVF Conference on Computer Vision and Pattern Recognition*, pages 26608–26617, 2025. 3
- [27] Haolin Liu, Yujian Zheng, Guanying Chen, Shuguang Cui, and Xiaoguang Han. Towards high-fidelity single-view holistic reconstruction of indoor scenes. In *European Conference on Computer Vision*, pages 429–446. Springer, 2022. 5, 6, 12, 13
- [28] Jian Liu, Jing Xu, Song Guo, Jing Li, Guojingfeng, Jiaao Yu, Haohan Weng, Biwen Lei, Xianghui Yang, Zhuo Chen, Fangqi Zhu, Tao Han, and Chunchao Guo. Mesh-RFT: Enhancing mesh generation via fine-grained reinforcement fine-tuning. In *The Thirty-ninth Annual Conference on Neural Information Processing Systems*, 2025. 3
- [29] Minghua Liu, Chao Xu, Haian Jin, Linghao Chen, Mukund Varma T, Zexiang Xu, and Hao Su. One-2-3-45: Any single image to 3d mesh in 45 seconds without per-shape optimization. *Advances in Neural Information Processing Systems*, 36:22226–22246, 2023. 1
- [30] Minghua Liu, Ruoxi Shi, Linghao Chen, Zhuoyang Zhang, Chao Xu, Xinyue Wei, Hansheng Chen, Chong Zeng, Jiayuan Gu, and Hao Su. One-2-3-45++: Fast single image to 3d objects with consistent multi-view generation and 3d diffusion. In *Proceedings of the IEEE/CVF Conference on Computer Vision and Pattern Recognition*, pages 10072–10083, 2024.
- [31] Ruoshi Liu, Rundi Wu, Basile Van Hoorick, Pavel Tokmakov, Sergey Zakharov, and Carl Vondrick. Zero-1-to-3: Zero-shot one image to 3d object. In *Proceedings of the IEEE/CVF International Conference on Computer Vision*, pages 9298–9309, 2023. 1, 2
- [32] Sainan Liu, Vincent Nguyen, Yuan Gao, Subarna Tripathi, and Zhuowen Tu. Towards panoptic 3d parsing for single image in the wild. *arXiv preprint arXiv:2111.03039*, 2021. 2
- [33] William E Lorensen and Harvey E Cline. Marching cubes: A high resolution 3d surface construction algorithm. In *Seminal graphics: pioneering efforts that shaped the field*, pages 347–353. Association for Computing Machinery, 1998. 2
- [34] Charlie Nash, Yaroslav Ganin, SM Ali Eslami, and Peter Battaglia. Polygen: An autoregressive generative model of 3d meshes. In *International conference on machine learning*, pages 7220–7229. PMLR, 2020. 2
- [35] Piotr Nawrot, Szymon Tworkowski, Michał Tyrolski, Łukasz Kaiser, Yuhuai Wu, Christian Szegedy, and Henryk Michalewski. Hierarchical transformers are more efficient language models. In *Findings of the Association for Computational Linguistics: NAACL 2022*, pages 1559–1571, 2022. 3
- [36] Maxime Oquab, Timothée Darcet, Théo Moutakanni, Huy V. Vo, Marc Szafraniec, Vasil Khalidov, Pierre Fernandez, Daniel HAZIZA, Francisco Massa, Alaaeldin El-Nouby, Mido Assran, Nicolas Ballas, Wojciech Galuba, Russell Howes, Po-Yao Huang, Shang-Wen Li, Ishan Misra, Michael Rabbat, Vasu Sharma, Gabriel Synnaeve, Hu Xu, Herve Jegou, Julien Mairal, Patrick Labatut, Armand Joulin, and Piotr Bojanowski. DINOv2: Learning robust visual features without supervision. *Transactions on Machine Learning Research*, 2024. Featured Certification. 5
- [37] Tianhe Ren, Shilong Liu, Ailing Zeng, Jing Lin, Kunchang Li, He Cao, Jiayu Chen, Xinyu Huang, Yukang Chen, Feng Yan, et al. Grounded sam: Assembling open-world models for diverse visual tasks. *arXiv preprint arXiv:2401.14159*, 2024. 5
- [38] Jarek Rossignac. Edgebreaker: Connectivity compression for triangle meshes. *IEEE Transactions on Visualization and Computer Graphics*, 5(1):47–61, 1999. 5
- [39] Yawar Siddiqui, Antonio Alliegro, Alexey Artemov, Tatiana Tommasi, Daniele Sirigatti, Vladislav Rosov, Angela Dai, and Matthias Nießner. Meshgpt: Generating triangle meshes with decoder-only transformers. In *Proceedings of the IEEE/CVF Conference on Computer Vision and Pattern Recognition*, pages 19615–19625, 2024. 2
- [40] Xingyuan Sun, Jiajun Wu, Xiuming Zhang, Zhoutong Zhang, Chengkai Zhang, Tianfan Xue, Joshua B Tenenbaum, and William T Freeman. Pix3d: Dataset and methods for single-image 3d shape modeling. In *Proceedings of the IEEE conference on computer vision and pattern recognition*, pages 2974–2983, 2018. 5, 7, 12, 13
- [41] Jiaxiang Tang, Zhaoshuo Li, Zekun Hao, Xian Liu, Gang Zeng, Ming-Yu Liu, and Qinsheng Zhang. Edgerunner: Auto-regressive auto-encoder for artistic mesh generation. In *The Thirteenth International Conference on Learning Representations*, 2025. 2, 3, 4, 13
- [42] Nanyang Wang, Yinda Zhang, Zhuwen Li, Yanwei Fu, Wei Liu, and Yu-Gang Jiang. Pixel2mesh: Generating 3d mesh models from single rgb images. In *Proceedings of the European Conference on Computer Vision (ECCV)*, pages 52–67, 2018. 2
- [43] Haohan Weng, Yikai Wang, Tong Zhang, C. L. Philip Chen, and Jun Zhu. Pivotmesh: Generic 3d mesh generation via pivot vertices guidance. In *The Thirteenth International Conference on Learning Representations*, 2025. 3
- [44] Haohan Weng, Zibo Zhao, Biwen Lei, Xianghui Yang, Jian Liu, Zeqiang Lai, Zhuo Chen, Yuhong Liu, Jie Jiang, Chunchao Guo, et al. Scaling mesh generation via compressive tokenization. In *Proceedings of the IEEE/CVF Conference on Computer Vision and Pattern Recognition*, pages 11093–11103, 2025. 2, 3, 4, 13
- [45] Haiyang Xu, Yu Lei, Zeyuan Chen, Xiang Zhang, Yue Zhao, Yilin Wang, and Zhuowen Tu. Bayesian diffusion models for

- 3d shape reconstruction. In *Proceedings of the IEEE/CVF Conference on Computer Vision and Pattern Recognition*, pages 10628–10638, 2024. [2](#)
- [46] Longwen Zhang, Ziyu Wang, Qixuan Zhang, Qiwei Qiu, Anqi Pang, Haoran Jiang, Wei Yang, Lan Xu, and Jingyi Yu. Clay: A controllable large-scale generative model for creating high-quality 3d assets. *ACM Transactions on Graphics*, 43(4):1–20, 2024. [1](#), [2](#)
- [47] Xiang Zhang, Zeyuan Chen, Fangyin Wei, and Zhuowen Tu. Uni-3d: A universal model for panoptic 3d scene reconstruction. In *Proceedings of the IEEE/CVF International Conference on Computer Vision*, pages 9256–9266, 2023. [1](#), [2](#), [6](#), [12](#), [13](#)
- [48] Xiang Zhang, Yawar Siddiqui, Armen Avetisyan, Chris Xie, Jakob Engel, and Henry Howard-Jenkins. Vertexregen: Mesh generation with continuous level of detail. In *Proceedings of the IEEE/CVF International Conference on Computer Vision*, pages 12570–12580, 2025. [2](#), [3](#)
- [49] Qingcheng Zhao, Xiang Zhang, Haiyang Xu, Zeyuan Chen, Jianwen Xie, Yuan Gao, and Zhuowen Tu. Depr: Depth guided single-view scene reconstruction with instance-level diffusion. In *Proceedings of the IEEE/CVF International Conference on Computer Vision*, pages 5722–5733, 2025. [1](#), [2](#), [3](#), [5](#), [6](#), [8](#), [12](#), [13](#)
- [50] Ruowen Zhao, Junliang Ye, Zhengyi Wang, Guangce Liu, Yiwen Chen, Yikai Wang, and Jun Zhu. Deepmesh: Auto-regressive artist-mesh creation with reinforcement learning. In *Proceedings of the IEEE/CVF International Conference on Computer Vision*, pages 10612–10623, 2025. [3](#)
- [51] Junsheng Zhou, Yu-Shen Liu, and Zhizhong Han. Zero-shot scene reconstruction from single images with deep prior assembly. *Advances in Neural Information Processing Systems*, 37:39104–39127, 2024. [1](#), [2](#), [3](#), [5](#), [6](#), [12](#), [13](#)

## A. Appendix

### A.1. Additional Implementation Details

#### A.1.1. Data Pre-processing

We pre-process meshes from the 3D-FRONT [14] dataset to ensure they are suitable for autoregressive tokenization.

- **Vertex Merging** We merge nearby vertices using a minimum spatial resolution determined by the quantization level  $q \in \{128, 256, 512, 1024\}$ , where the minimum resolution is  $1/q$ .
- **Mesh Simplification** We apply planar decimation followed by quadric-error-based edge-collapse decimation with target face counts of 800, 2000, and 4000.
- **Quality Selection** We compute the Hausdorff distance between the simplified meshes and the originals, thresholding with an empirical value  $\tau = 0.01$ . If the distance is below  $\tau$ , we choose the mesh with fewer faces; otherwise, we select the quantization level and decimation setting that produce the lowest Hausdorff distance. This procedure balances compactness and geometric fidelity.

The resulting processed dataset contains meshes with an average of 1,809 faces per shape.

#### A.1.2. Training Details

To enhance layout prediction accuracy, we employ a two-stage training strategy:

- **Layout Bootstrapping** We first train the model exclusively on the layout prediction prefix tokens. This stage consists of 100k iterations for the EdgeRunner-based variant and 30k iterations for the BPT-based model.
- **Joint Pose-Mesh Training** Building on the bootstrapped weights, we train the model on the full pose and mesh sequence. This final stage requires 30k iterations for EdgeRunner and 25k iterations for BPT.

Both stages utilize the AdamW optimizer with an initial learning rate of  $1 \times 10^{-4}$ , featuring a 500-step linear warmup followed by a cosine decay to  $1 \times 10^{-5}$ . Training is conducted with an effective batch size of 64. We set the optimizer hyperparameters to  $\beta_1 = 0.9$  and  $\beta_2 = 0.95$ , and apply gradient clipping at a threshold of 1.0.

## A.2. Additional Results

### A.2.1. More Qualitative Results on Real Images

We present additional qualitative results on real indoor scenes from Pix3D [40], Matterport3D [3] and ScanNet [11] in Fig. A.1. Across diverse environments and lighting conditions, PixARMesh generally achieves stronger layout alignment and produces coherent scene reconstructions, while retaining the advantages of compact, artist-ready mesh outputs.

Method	$ F $	$ V $
InstPIFu [27]	1,942,029	970,951
Uni-3D [47]	141,130	70,844
BUOL [8]	55,493	27,750
Gen3DSR [13]	364,285	216,797
DeepPriorAssembly [51]	250,875	125,420
MIDI [19]	1,936,248	967,886
DepR [49]	319,646	159,905
<b>PixARMesh-EdgeRunner (Ours)</b>	7,110	4,253
<b>PixARMesh-BPT (Ours)</b>	7,506	4,050

Table A.1. Face count  $|F|$  and vertex count  $|V|$  comparisons.

### A.2.2. Face and Vertex Counts

As shown in Tab. A.1, we report the average number of faces and vertices per reconstructed scene across different methods. InstPIFu [27] and MIDI [19] produce extremely dense outputs, requiring roughly 2M faces per scene. BUOL [8], Gen3DSR [13], and DeepPriorAssembly [51] reduce this to about 0.3M faces, though still far from mesh-efficient. In contrast, PixARMesh produces dramatically more compact meshes, *i.e.* around 7–8k faces depending on the base model, while maintaining competitive geometric quality. This highlights the practical advantage of generating artist-ready, natively structured meshes rather than relying on iso-surface extraction.

### A.2.3. Object Pose (Layout) Accuracy

Method	GT Depth	Box IoU (%)
MIDI [19]	–	31.07
DepR [49]		33.98
DepR [49]	✓	36.67
<b>PixARMesh-EdgeRunner (Ours)</b>		56.76
<b>PixARMesh-EdgeRunner (Ours)</b>	✓	70.37
<b>PixARMesh-BPT (Ours)</b>		54.54
<b>PixARMesh-BPT (Ours)</b>	✓	65.01

Table A.2. Layout accuracy comparisons.

Following MIDI [19], we evaluate scene layout accuracy using the 3D bounding-box IoU between predictions and ground truth. For this setting, we use ground-truth instance masks to isolate layout estimation from segmentation errors. Results are reported in Tab. A.2. PixARMesh achieves higher layout accuracy than prior methods that rely on predicted depth, and we observe that the EdgeRunner-based variant consistently produces more accurate layouts than the BPT-based model.

### A.2.4. Runtime Analysis

We measure inference runtime on a single NVIDIA A100 GPU and report the average per-scene latency in Tab. A.3. Due to its autoregressive decoding process, PixARMesh is inherently slower than feed-forward approaches (InstPIFu [27], Uni-3D [47], BUOL [8]) as well as the latent-diffusion-based DepR [49]. Nonetheless, PixARMesh remains generally faster than other compositional pipelines such as Gen3DSR [13], while uniquely providing artist-

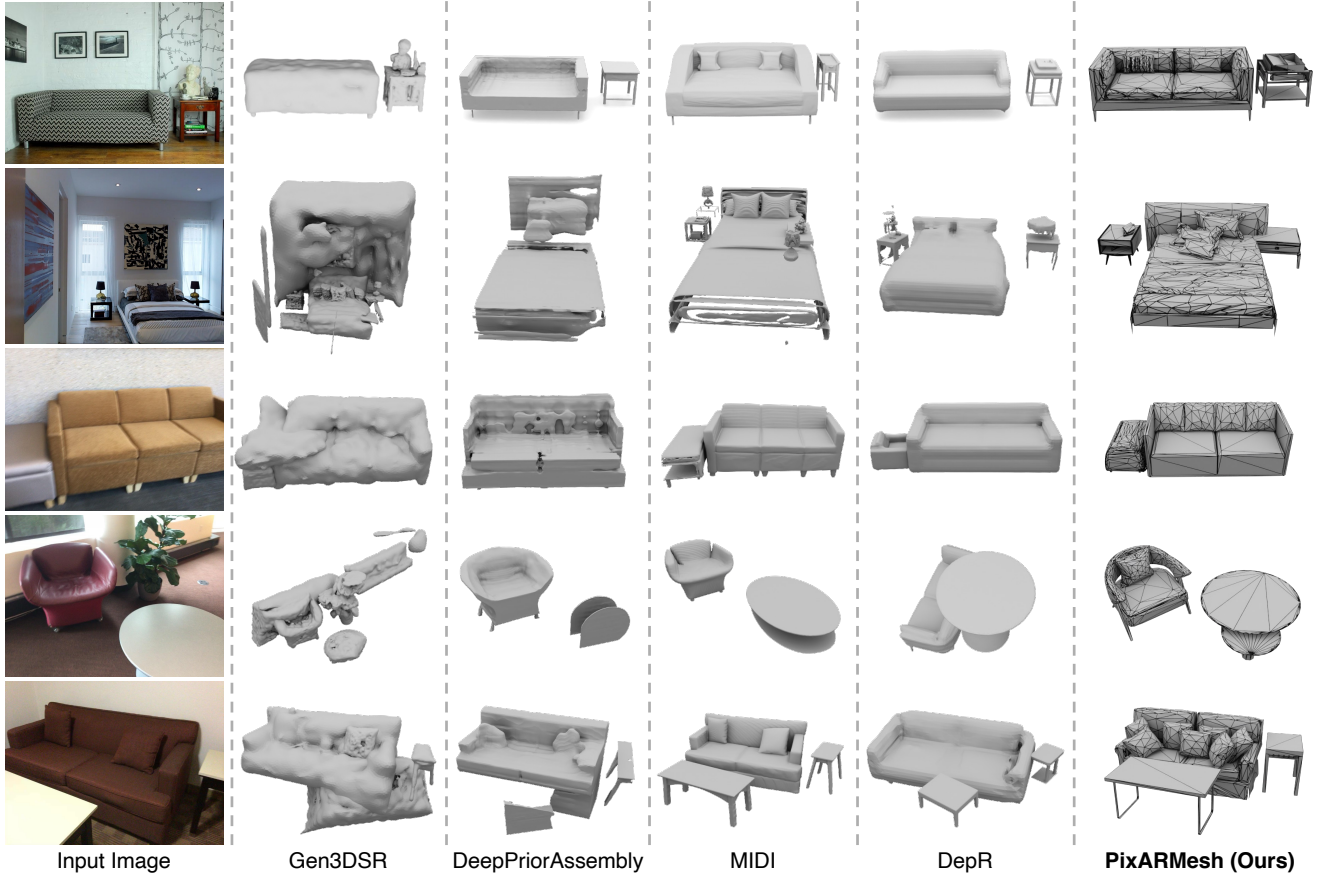


Figure A.1. Additional qualitative results on real images from Pix3D [40], Matterport3D [3] and ScanNet [11].

ready native mesh outputs without needing iso-surface extraction.

Method	Runtime
InstPIFu [27]	19.8 s
Uni-3D [47]	3.1 s
BUOL [8]	6.5 s
Gen3DSR [13]	15.5 min
DeepPriorAssembly [51]	6.7 min
MIDI [19]	1.6 min
DepR [49]	1.2 min
<b>PixARMesh-EdgeRunner (Ours)</b>	4.5 min
<b>PixARMesh-BPT (Ours)</b>	6.7 min

Table A.3. Inference runtime comparisons.

### A.2.5. BPT-Based Ablation Studies

To further assess the generality of our point-cloud encoder designs, we conduct additional ablations using the BPT-based mesh generative model [44], as summarized in Tab. A.4. The trends mirror those observed with EdgeRunner [41]: incorporating scene-level context aggregation without pixel-aligned features slightly reduces object-level fidelity but improves global alignment in the assembled scene. Introducing image features provides a substantial boost in scene-level accuracy, and adding our scene-level

context aggregation on top yields further gains. These results confirm that our proposed encoder designs remain effective across different mesh tokenizations and generative backbones.

Img Feat	Ctx Agg	Scene-level		F-Score	Object-level	
		CD ( $\times 10^{-3}$ , $\downarrow$ )	CD-S ( $\times 10^{-3}$ , $\downarrow$ )		CD ( $\times 10^{-3}$ , $\downarrow$ )	F-Score (%, $\uparrow$ )
		68.36	25.43	35.96	5.34	76.54
	✓	56.80	23.49	37.98	5.85	76.31
✓		57.03	23.70	41.51	<b>4.25</b>	<b>81.25</b>
✓	✓	<b>49.82</b>	<b>22.06</b>	<b>42.18</b>	4.57	80.30

Table A.4. Ablation studies on our point-cloud encoder design with BPT-based model. *Img Feat*, *Ctx Agg* denote pixel-aligned image features and scene context aggregation, respectively.